



HAL
open science

Investigation Into Debonding of Single Polypropylene Fiber Pullout in Concrete Using X-Ray Microtomography and Mechanically Regularized Digital Volume Correlation

Yujie Bi, Haizhou Liu, Lingtao Mao, Jiaojiao Liu, Yifan Liu, Jianmin Zuo,
Yang Ju, François Hild

► **To cite this version:**

Yujie Bi, Haizhou Liu, Lingtao Mao, Jiaojiao Liu, Yifan Liu, et al.. Investigation Into Debonding of Single Polypropylene Fiber Pullout in Concrete Using X-Ray Microtomography and Mechanically Regularized Digital Volume Correlation. *Materials and structures*, 2024, 57, pp.188. 10.1617/s11527-024-02466-z . hal-04691909

HAL Id: hal-04691909

<https://hal.science/hal-04691909v1>

Submitted on 9 Sep 2024

HAL is a multi-disciplinary open access archive for the deposit and dissemination of scientific research documents, whether they are published or not. The documents may come from teaching and research institutions in France or abroad, or from public or private research centers.

L'archive ouverte pluridisciplinaire **HAL**, est destinée au dépôt et à la diffusion de documents scientifiques de niveau recherche, publiés ou non, émanant des établissements d'enseignement et de recherche français ou étrangers, des laboratoires publics ou privés.

1 **Investigation Into Debonding of Single Polypropylene Fiber Pullout**
2 **in Concrete Using X-Ray Microtomography and Mechanically**
3 **Regularized Digital Volume Correlation**

4 Yujie Bi¹, Haizhou Liu², Lingtao Mao^{1, 3*}, Jiaojiao Liu¹, Yifan Liu⁴, Jianmin Zuo⁵,
5 Yang Ju³ and François Hild⁶

6 1. *School of Mechanics and Civil Engineering, China University of Mining & Technology,*
7 *Beijing 100083, China*

8 2. *Shenzhen Institute of Advanced Technology, Chinese Academy of Sciences, Shenzhen*
9 *518055, China*

10 3. *State Key Laboratory for Fine Exploration and Intelligent Development of Coal Resources,*
11 *China University of Mining & Technology, Beijing 100083, China*

12 4. *China Construction Seventh Engineering Division Corp., Ltd., Zhengzhou, 450000, China*

13 5. *Beijing YJK Building Software Co., Ltd, Beijing 100029, China*

14 6. *Université Paris-Saclay, CentraleSupélec, ENS Paris-Saclay, CNRS, LMPS - Laboratoire de*
15 *Mécanique Paris-Saclay, 91190 Gif-sur-Yvette, France*

16 * Corresponding author: mlt@cumtb.edu.cn;

17 **Abstract**

18 To investigate the debonding process, an in-situ pullout experiment on an indented single
19 polypropylene fiber was conducted using X-ray microtomography. This study utilized mechanically
20 regularized global digital volume correlation (Reg-G-DVC) to measure the deformation fields of
21 the fiber, matrix, and interfaces during interfacial debonding. Reg-G-DVC mitigates the impact of
22 low contrast on measurement uncertainties, ensures the convergence of DVC calculations, and
23 enables the element size to be reduced to improve the spatial resolution. The displacement jumps of
24 the shared nodes between the fiber and the matrix were used to quantify interfacial debonding. The
25 profiles of the normal and tangential components of the displacement jumps exhibited periodic
26 features corresponding to the geometry of the indented fiber as it was pulled out. Additionally, the
27 force-displacement curves displayed multi-peak fluctuations corresponding to the fiber geometry,
28 thereby indicating that the periodic indentation of the fiber enhanced friction and the cohesive force
29 between the fiber and the matrix during the pullout process. The displacement jumps along the fiber
30 was maximum at the embedded initiation and decreased along the fiber toward the embedded end.

31 The aforementioned research demonstrated the advantages of utilizing Reg-G-DVC in measuring
32 displacement fields during interfacial debonding, which provides deformation data for identifying
33 and validating interface models.

34

35

36 **Keywords:** Fiber; Debonding; DVC measurements; CT analysis.

37

38 **1 Introduction**

39 Fiber-reinforced concrete (FRC) exhibits high toughness, ductility, impact resistance, and
40 fatigue resistance. In recent years, it has been widely employed in various engineering fields
41 including residential construction [1,2], bridge structures [3,4], pavements [5,6], and tunnel
42 linings [7-10] to cite a few. In FRCs, the fibers are interconnected with the cement/mortar matrix
43 through interfaces. When the material undergoes tensile loading and the matrix begins to crack, the
44 load is transmitted through the interface to the fibers. The fibers share the tensile load, thus
45 preventing further cracking of the matrix and enhancing the tensile strength of the material. In this
46 process, the matrix strength determines that of the material, whereas the mechanical characteristics
47 of the interface affect the reinforcement, toughening, and crack resistance of the fibers in the matrix.
48 Research indicates that the stress states between the fibers and the matrix in single-fiber pullout tests
49 are similar to those between bridging fibers and the cracking matrix during the cracking process of
50 FRCs [11]. Additionally, the shear stress–slip relationship observed experimentally is considered an
51 intrinsic property of the interface. Hence, scholars have investigated the mechanical bonding
52 characteristics of interfaces via fiber pullout experiments and numerical simulations [12-14]. They
53 have utilized parameters such as the pullout peak load, bonding strength, and pullout work to
54 characterize the bonding performance. These studies investigated the effects of factors such as fiber
55 type [15,16], surface features [17], embedment angle [18,19], matrix strength [19], and amount of
56 matrix constituents [20] on the interface bonding performance to infer interface damage and failure
57 conditions.

58 Fibers typically used in FRCs can be classified into three main categories: i) metal fibers (i.e.,
59 primarily steel fibers); ii) inorganic material fibers (i.e., generally glass or basalt fibers); and
60 iii) organic synthetic fibers (e.g., polypropylene, polyamide, polyester, polyacrylonitrile, and
61 polyvinyl alcohol fibers). Among them, the steel fibers have the widest application spectrum.
62 However, their high weight and cost, along with the potential issue of tire punctures when fibers
63 protrude from surfaces, as reported in airports and highway pavements [21-23], have prompted the
64 search for alternative reinforcement materials. Synthetic fibers, which is a novel type of
65 reinforcement material, have rapidly developed and are utilized in concrete owing to their low cost,
66 high strength, good elasticity, wear resistance, and corrosion resistance [24-26]. Studying the

67 interface bonding and slip mechanisms of synthetic fiber concrete may provide a theoretical basis
68 for the design of synthetic fiber concrete.

69 Most studies regarding synthetic FRCs have primarily focused on the macroscopic mechanical
70 characteristics of fiber pullout [27-29]. In these studies, the pullout process was observed on a two-
71 dimensional scale and the interface bonding and sliding processes between the matrix and fibers
72 were inferred [30]. However, in reality, interface bonding and sliding are complex three-dimensional
73 phenomena, and analyzing them solely from a two-dimensional perspective cannot accurately
74 capture the mechanical performance of interfaces. Therefore, a method to measure the internal
75 deformation of a material on a three-dimensional scale must be identified and the interface bonding
76 and sliding processes analyzed. Optical measurement methods such as photoelasticity [31], digital
77 image correlation (DIC) [32-34], and digital gradient sensing [35] offer advantages such as full-
78 field coverage, noncontact nature, and visual interpretation, thus rendering them useful for assessing
79 stress or strain fields at interfaces and in matrices. However, methods such as photoelasticity and
80 digital gradient sensing require materials with photoelastic properties, and DIC is primarily used for
81 surface measurements. Although these methods have revealed some key aspects of the force
82 characteristics during pullout tests, they do not comprehensively capture three-dimensional features
83 at interfaces between fibers and cementitious matrices.

84 X-ray microtomography is a nondestructive and noncontact testing technique that has been
85 widely applied to observe the internal characteristics of concrete and to establish detailed numerical
86 models [36-38]. Derived from two-dimensional DIC, digital volume correlation (DVC) [39,40]
87 combined with X-ray microtomography is applied to investigating three-dimensional deformation
88 fields in specimens. Yang et al. [41], Mao et al. [42] and Chateau et al. [43] employed DVC to
89 analyze local deformations before crack initiation in concrete specimens under uniaxial compression,
90 which provided insights into early stage microcracks, which are difficult to distinguish directly via
91 microtomography imaging. Stamati et al. [44] used DVC to measure internal deformation fields and
92 their evolution in concrete specimens subjected to uniaxial and triaxial compression. Flansbjer et
93 al. [45] combined microtomography with DVC to capture the deformation field during pullout of
94 hooked-end steel fibers from a cementitious matrix, and studied the load transfer mechanism. In
95 these studies, the DVC method involved subsets whose length typically comprised tens of voxels,
96 which was much larger than the scale used in interface studies. The spatial resolution of DVC limits

97 its ability to precisely measure the deformation in interface areas. Hild et al. [46] and Leclerc et al.
98 [47] introduced mechanically regularized global DVC (Reg-G-DVC) based on the equilibrium gap.
99 This method not only ensures lower measurement uncertainties, but also enhances the spatial
100 resolution of displacement field measurements, possibly to the voxel level. Tsitova et al. [48]
101 considered the heterogeneity of the material and used this method to measure the strain field of
102 mortar specimens under three-point bending experiments, and quantified three damage mechanisms.
103 Riccardi et al. [49] used this method to analyze the debonding of fiber-reinforced polymer anchors
104 in concrete during bending tests and described how the material degradation developed in the anchor
105 region. Jänicke et al. [50] employed Reg-G-DVC to quantify debonding of fibers embedded in two
106 brittle matrices, measured the relative motion at the interface, and analyzed the load-transfer
107 mechanism between the fiber and matrix.

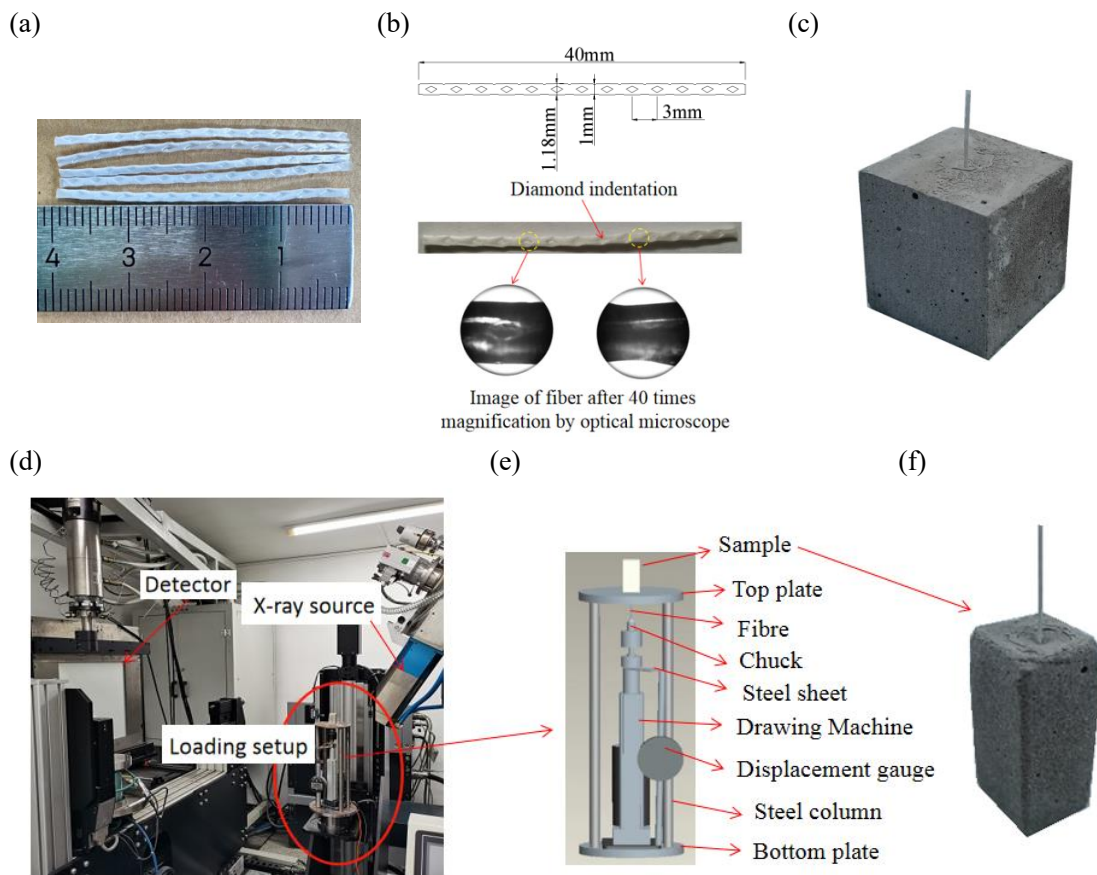
108 Due to the addition of mechanical regularization, Reg-G-DVC allows for the use of finer mesh
109 sizes, thereby enhancing the spatial resolution of kinematic measurements, which improves the
110 measurements of displacements at interfaces between fibers and matrices. In this paper, the
111 displacement field and debonding process of the interface between a polypropylene fiber and a
112 cementitious matrix were studied by using Reg-G-DVC combined with an in-situ pullout test
113 scanned via microtomography. Section 2 introduces the experimental setup and procedures. Section
114 3 provides an analysis of the equivalent speckle size of the imaged sample as well as the
115 measurement uncertainty, and determines the DVC calculation parameters. Section 4 discusses the
116 measurement results, analyzes the displacement and gray level residual fields for different load
117 levels, as well as the debonding state of the interface between the fiber and the matrix.

118 **2 Materials and Methods**

119 **2.1 Specimens and Experimental Setup**

120 The matrix material employed for the investigated specimens was ordinary Portland cement
121 (P.O.42.5, Datong, Shanxi, China). Fine aggregates were used (Zone II sand) with a fineness
122 modulus of 2.81. The cement–mortar mix proportion was cement : water : sand = 1:0.45:1. The fiber
123 utilized herein was tunnel lining spray concrete-specific, of indentation-type, and high-strength. It
124 was a modified polypropylene coarse fiber produced by Ningbo Shike New Materials Technology

125 Co., Ltd. (Fig. 1(a)). It had a length of 40 mm, a cross-sectional width of 1 mm, and a thickness of
 126 0.66 mm. The fiber surface featured diamond-shaped indentations with a spacing of 3 mm, and a
 127 depth of 0.2 mm. The maximum width of the fiber section was 1.18 mm at indentation locations. Its
 128 structure and images magnified $40\times$ (using an optical microscope) are shown in Fig. 1(b). The
 129 indentation increased the cohesive strength and friction force between the fiber and the matrix when
 130 the fiber was pulled out.
 131



132 Fig. 1 Specimens and Experimental setup. (a) Polypropylene fibers. (b) Structural diagram and
 133 magnified sections of a Polypropylene fiber. (c) Specimens for fiber pullout experiments (40 mm
 134 \times 40 mm \times 40 mm). (d) CT System for in-situ fiber pullout. (e) Schematic illustration of pullout
 135 experiments. (f) Specimens for in-situ fiber pullout experiments (20 mm \times 20 mm \times 40 mm).

136 The mechanical parameters of the matrix were obtained via uniaxial compression tests. The
 137 Young's modulus was equal to 29 GPa, Poisson's ratio was 0.16, and the compressive strength was
 138 29 MPa. The mechanical parameters of the fiber were provided by the manufacturer (i.e., Young's
 139 modulus: 7.2 GPa, Poisson's ratio: 0.35, failure strength: 715 MPa, elongation at failure: 14%).

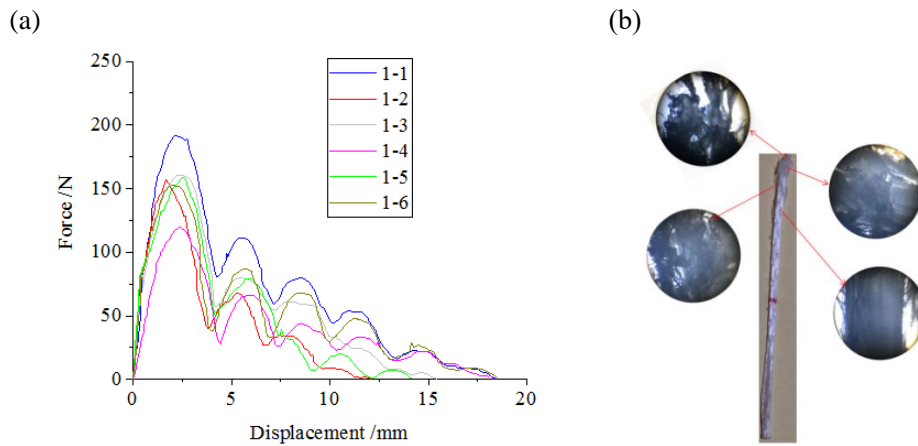
140 Cubic mortar specimens of size 40 mm × 40 mm × 40 mm were prepared for fiber pullout
141 experiments. A polypropylene fiber was embedded at the center of each specimen down to a depth
142 of 15 mm (Fig. 1(c)).

143 The microtomography system used for the experiment was equipped with an YXLON 225 kV
144 microfocus X-ray source and an XRD 1611 AP3 flat-panel detector with a definition of
145 2048 × 2048 pixels. A custom-designed experimental setup was developed for in-situ
146 microtomography scanning of fiber pullout. This setup comprised a main support frame, driving
147 motor (maximum pulling force = 2000 N, and loading speed = 0.28 mm/s), load sensor (range = 0
148 to 3 kN, and standard uncertainty = 9 N), and displacement sensor (range = 0 to 50 mm, and standard
149 uncertainty = 10 μm). During the experiment, the setup was fixed to the turntable of the
150 microtomography system. Fig. 1(d) shows the setup for in-situ single-fiber pullout test, and Fig. 1(e)
151 schematically illustrates the pullout setup. To minimize X-ray attenuation, the samples were further
152 prepared via wire cutting into 20 mm × 20 mm × 40 mm cubes, which were more suitable for in-
153 situ microtomography scanning (Fig. 1(f)).

154 **2.2 Single-Fiber Pullout Experiment**

155 Pullout experiments were conducted on six specimens, and the corresponding force–
156 displacement curves are shown in Fig. 2(a). The maximum, minimum, and average pullout peak
157 loads were 190, 120, and 153 N, respectively. The force–displacement curves exhibited multipeak
158 characteristics, which are related to the geometry of the indented fiber (Fig. 1). The larger cross-
159 sectional width at the indentation location increases mechanical interlocking and friction forces
160 between the fiber and the matrix during pullout, thus resulting in periodic increases and decreases
161 in the reported forces. The distance between the peaks and corrugation spacing is approximately
162 3 mm, whereas the load at the peak gradually decreases as the pullout length increases. The
163 magnified morphology of the fiber after pullout observed under an optical microscope at 40 ×
164 magnification is shown in Fig. 2(b). It revealed scratches on the fiber surface. The embedded
165 initiation of the fiber indicated less damage, whereas the embedded end showed severe damage with
166 burrs appearing on the surface, similar to those observed in post-abrasion.

167



168 Fig. 2. Polypropylene fiber pullout results. (a) Force–displacement curves of specimens.

169 (b) Morphology of a fiber after its pullout.

170 Based on the afore-reported pullout curves, an in-situ pullout experiment was conducted. The
 171 force–displacement curve is shown in Fig. 3(a). After the load application ceased, force relaxations
 172 occurred and the scanning was conducted once stability was achieved. The green “x” positions on
 173 the curve indicate dwell points during loading, whereas the red circles depict the scanning points.
 174 The latter ones correspond to forces equal to 0 N (unloaded), 56 N (dwell force of 126 N), 86 N
 175 (dwell force of 161 N), 46 N after the peak load, and 0 N after the peak load. The reconstructed
 176 volume size was $1200 \times 1200 \times 1380$ voxels, and each voxel corresponded to a physical size of 19
 177 $\mu m \times 19 \mu m \times 19 \mu m$. The experiment was conducted at a beam voltage of 130 kV and a current
 178 of 0.4 mA for 20 min. 1,200 projections were acquired over a 360° revolution. The images were
 179 encoded over an 8-bit grayscale.

180

181

182

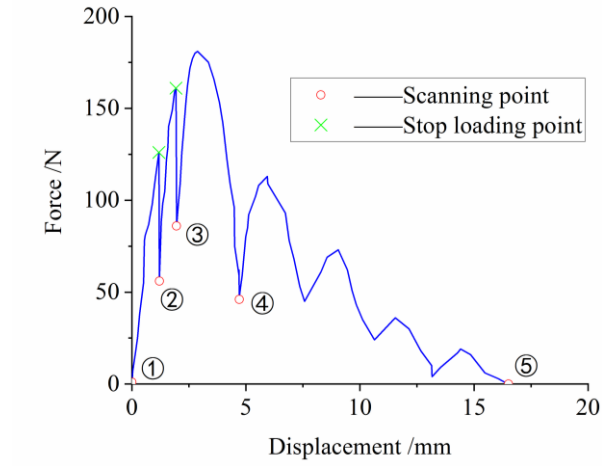
183

184

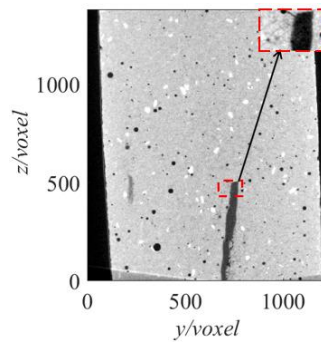
185

186

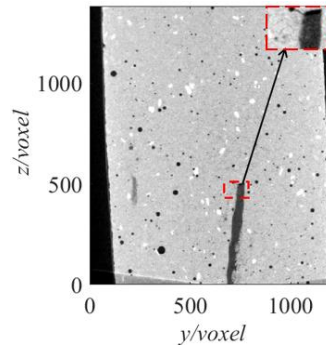
(a)



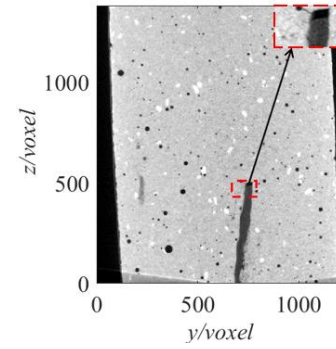
(b)



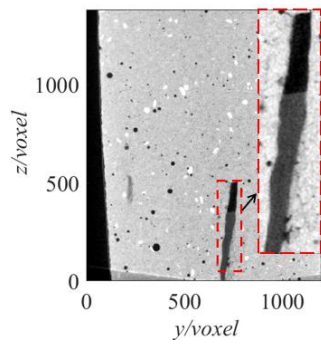
(c)



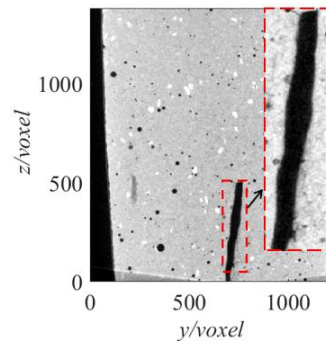
(d)



(e)



(f)



187

188 Fig. 3 Force–displacement curve for the in-situ pullout test and middle sections of steps 1 to 5.

189 (a) Force–displacement curve. (b) Step 1 (0N), (c) step 2 (126 N), (d) step 3 (161N), (e) step 4

190 (after peak load, 46 N) and (f) step 5 (after peak load, 0 N) sections.

191

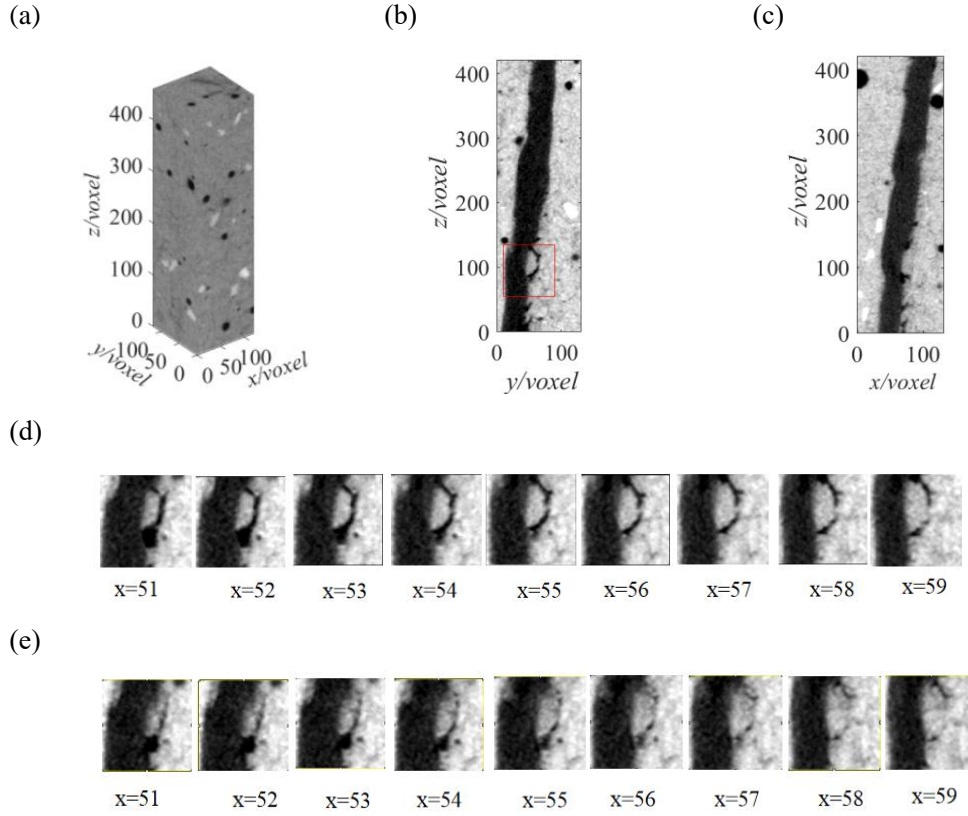
192 Fig. 3(b) shows a middle section including the fiber with no applied load, and those with a

193 partially enlarged red box area of the fiber end at each loading stage are shown in Fig. 3(c,f),
194 respectively. With the aid of Fiji software [51], it was evaluated that approximately 3 voxels (57
195 μm) of the fiber were pulled out from the embedded end when the force was equal to 126 N
196 (Fig. 3(c)). When the pullout force reached 161 N (Fig. 3(d)), approximately 13 voxels (247 μm)
197 of the fiber were removed from the embedded end. Partial debonding of the fiber is observed in this
198 region, although the pullout load had not yet reached its peak level. The load was increased until it
199 reached its ultimate value. Then, at a load of 46 N after the peak, approximately 140 voxels (2660
200 μm) of the fiber were pulled out (Fig. 3(e)), and in the final stage, the fiber was completely pulled
201 out (Fig. 3(f)).

202 Throughout the pullout process, after the peak load was reached, the pullout curve exhibited
203 the same characteristics as the reference single fiber pullout experiments (i.e., multipeak features
204 associated with indentation spacing). Additionally, Fig. 3 shows that the fiber was orientated at an
205 angle of ca. 7.5° in this section plane along the z-axis. This inclination angle may affect the pullout
206 behavior.

207 Owing to significant artifacts near the lower portion of the specimen close to the supporting
208 top platen, and the limited effect of the upper part distant from the fiber extraction end, a VOI
209 comprising 421 layers of images that spanned 80 pixels upward from the fiber-embedded initiation
210 region to 500 pixels into the interior of the cement matrix. To avoid too heavy computations, the
211 region depicted in Fig. 4(a) was selected. It comprised $130 \times 130 \times 421$ voxels and served as the
212 VOI. Fig.4(b) and (c) respectively show the yOz section at $x = 55$ voxels, and xOz section at $y = 50$
213 voxels. The enlarged image of the red box area section ($x=55$ voxels) and its adjacent 8-layer
214 sections ($x = 51\sim 54$ voxels, $x = 56\sim 59$ voxels) are shown in Fig. 4(d). The corresponding sections
215 in this area under a pull-out load of 126 N are displayed in Fig. 4(e). Based on a comparison between
216 Figs. 4(d) and (e), when the fiber was pulled out, pores and cracks in the nearby matrix closed,
217 which was caused by the inclined embedding of the fiber, thus resulting in lateral stresses on the
218 matrix.

219
220
221
222



223 Fig. 4 Effect of fiber pullout on the matrix. (a) DVC calculation region (VOI). (b) yOz sections at
 224 $x = 55$ voxels for the unloaded state. (c) Corresponding xOz sections at $y = 50$ voxels.
 225 (d) Magnified views of sections when the applied force is equal to 0 N. (e) Corresponding sections
 226 when the applied load was equal to 126 N.
 227

228 2.3 Regularized Global DVC

229 In this study, Reg-G-DVC was employed to measure displacement fields. The underlying
 230 principle of this method is as follows. The reference and deformed volumes correspond to f and
 231 g , respectively. Under the assumption of grayscale conservation, the displacement field $\mathbf{u}(\mathbf{x})$ is
 232 determined by minimizing the sum of squared differences

$$\min_{\{\mathbf{u}\}} \Phi_c^2 = \sum_{\text{VOI}} [f(\mathbf{x}) - g(\mathbf{x} + \mathbf{u}(\mathbf{x}))]^2 \quad (1)$$

233 where volume of interest (VOI) represents the selected region within the reference volume. Similar
 234 to the discretization of finite-element models, the displacement of any point within an element is
 235 expressed in terms of nodal displacements u_i , which are gathered in the column vector $\{\mathbf{u}\}$, and
 236 corresponding shape functions $\mathbf{N}_i(\mathbf{x})$

$$\mathbf{u}(\mathbf{x}) = \sum_i u_i \mathbf{N}_i(\mathbf{x}) \quad (2)$$

237 The gray residual φ_c is defined as the absolute difference in gray levels between the reference
 238 volume and the deformed volume corrected by the measured displacement field $\mathbf{u}(\mathbf{x})$

$$\varphi_c(\mathbf{x}) = |f(\mathbf{x}) - g(\mathbf{x} + \mathbf{u}(\mathbf{x}))| \quad (3)$$

239 and the dimensionless correlation residual ρ_{dvc} is defined as

$$\rho_{dvc} = \frac{1}{(\max(f(\mathbf{x})) - \min(f(\mathbf{x})))} \sqrt{\frac{1}{\text{VOI}} \sum (f(\mathbf{x}) - g[\mathbf{x} + \mathbf{u}(\mathbf{x})])^2} \quad (4)$$

241 Using a Gauss-Newton scheme, the minimization problem expressed in Equation (1) is
 242 transformed into an iterative solution to linear systems of equations

$$[\mathbf{M}]\{\mathbf{du}\} - \{\mathbf{b}\}^i = \{\mathbf{0}\} \quad (5)$$

243 with

$$b_m^i = \int_{\text{VOI}} (\nabla f(\mathbf{x}) \cdot \mathbf{N}_m(\mathbf{x})) (f(\mathbf{x}) - g(\mathbf{x} + \mathbf{u}^i(\mathbf{x}))) \mathbf{dx} \quad (6)$$

$$M_{mm} = \int_{\text{VOI}} (\nabla f(\mathbf{x}) \cdot \mathbf{N}_m(\mathbf{x})) (\nabla f(\mathbf{x}) \cdot \mathbf{N}_n(\mathbf{x})) \mathbf{dx} \quad (7)$$

$$\mathbf{du} = \mathbf{u}^{i+1} - \mathbf{u}^i \quad (8)$$

244 where $[\mathbf{M}]$ is the DVC Hessian matrix, \mathbf{du} the iterative displacement increment.

245 A regularization approach can be used to address the ill-posed problem of DVC by introducing
 246 a penalty function. According to linear elasticity, the equilibrium equations in a finite-element sense
 247 read

$$[\mathbf{K}]\{\tilde{\mathbf{u}}\} = \{\mathbf{f}\} \quad (9)$$

248 where $[\mathbf{K}]$ is the global stiffness matrix, $\{\tilde{\mathbf{u}}\}$ the mechanically admissible nodal displacement
 249 vector, and $\{\mathbf{f}\}$ the nodal force vector. By substituting the measured values $\{\mathbf{u}\}$ into the previous
 250 equation, the equilibrium residual, which is also known as the equilibrium gap, is expressed as

$$\{\mathbf{f}_r\} = [\mathbf{K}]\{\mathbf{u}\} - \{\mathbf{f}\} \quad (10)$$

251 Without considering body forces, the internal nodes experience zero externally applied forces.
 252 Therefore, the displacement $\{\mathbf{u}\}$ should minimize the L2 norm of the mechanical residual forces

$$\Phi_m^2 = \{\mathbf{u}\}^T [\mathbf{K}]^T [\mathbf{K}]\{\mathbf{u}\} \quad (11)$$

253 Introducing Equation (11) as a penalty term into Equation (1), the nodal displacement vector $\{\mathbf{u}\}$

254 minimizes the weighted sum of the correlation residual Φ_c^2 and force residual Φ_m^2 . To make the
 255 two cost functions dimensionless, a plane waveform is considered

$$\tilde{\Phi}_m^2 = \frac{\Phi_m^2}{\{\mathbf{v}\}^T [\mathbf{K}]^T [\mathbf{K}] \{\mathbf{v}\}}, \tilde{\Phi}_c^2 = \frac{\Phi_c^2}{\{\mathbf{v}\}^T [\mathbf{M}] \{\mathbf{v}\}}, \quad (12)$$

256 where $\mathbf{v} = \mathbf{v}_0 e^{i\mathbf{k} \cdot \mathbf{x}}$ represents the displacement field of a plane waveform, \mathbf{v}_0 the displacement
 257 amplitude vector, and \mathbf{k} the wavevector. The total cost function Φ_t is written as [47]

$$\Phi_t^2 = \tilde{\Phi}_c^2 + \omega \tilde{\Phi}_m^2 \quad (13)$$

$$\omega = (2|\mathbf{k}| \pi \ell_{reg})^4 \quad (14)$$

258 where ω denotes the regularization weight, and ℓ_{reg} the regularization length. Introducing the
 259 equilibrium residual as a penalty provides a significant smoothing effect for high-frequency
 260 oscillating fields that are not mechanically admissible. Equation (13) is minimized using a Gauss-
 261 Newton scheme and the nodal displacements are measured.

262 **3 Uncertainty Analysis and Determination of Calculation Parameters**

263 **3.1 Analysis of Equivalent Speckle Size in FRC**

264 When measuring deformations using DVC, the microstructure of both fiber and matrix in the
 265 FRC serves as carrier of kinematic information, which directly affects the reliability of displacement
 266 calculations. The regions corresponding to the matrix and the fiber were selected separately, as
 267 shown in Fig. 5(a) and (b). The image shows that the gray level distribution was confined within
 268 relatively narrow ranges, thus indicating the absence of ideal contrast. The effect of the fiber pullout
 269 process on the upper region of the specimen was minimal, and the deformation in this region
 270 between the two scans was negligible. Consequently, the correlation residual φ_c in Equation (3) of
 271 this region can be regarded as due acquisition noise and reconstruction artifacts (Fig. 5(c)).

272

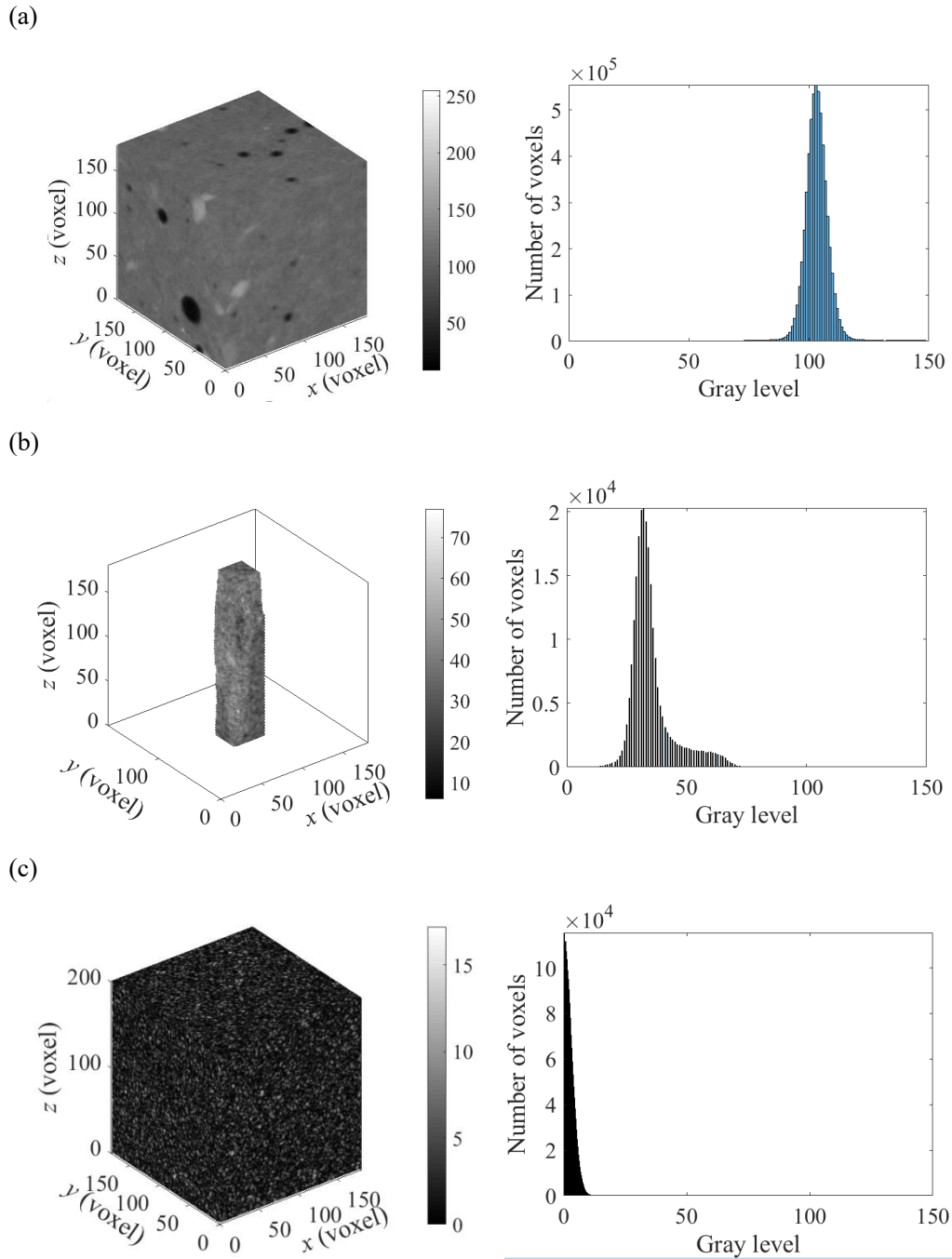
273

274

275

276

277



278 Fig. 5 Gray level images and histograms of three regions of interest. (a) Matrix, (b) Fiber,
 279 (c) Noise.

280
 281 According to the autocorrelation calculation, the equivalent speckle diameters of the fiber,
 282 matrix, and noise are 8.2, 6.6, and 2.6 voxels, respectively. The equivalent speckle sizes of both the
 283 fiber and the matrix in the reference image exceeded those of noise. This observation indicates that
 284 the contrast in the image was predominantly affected by material heterogeneities instead of noise,
 285 thereby ensuring the effectiveness of DVC measurements.

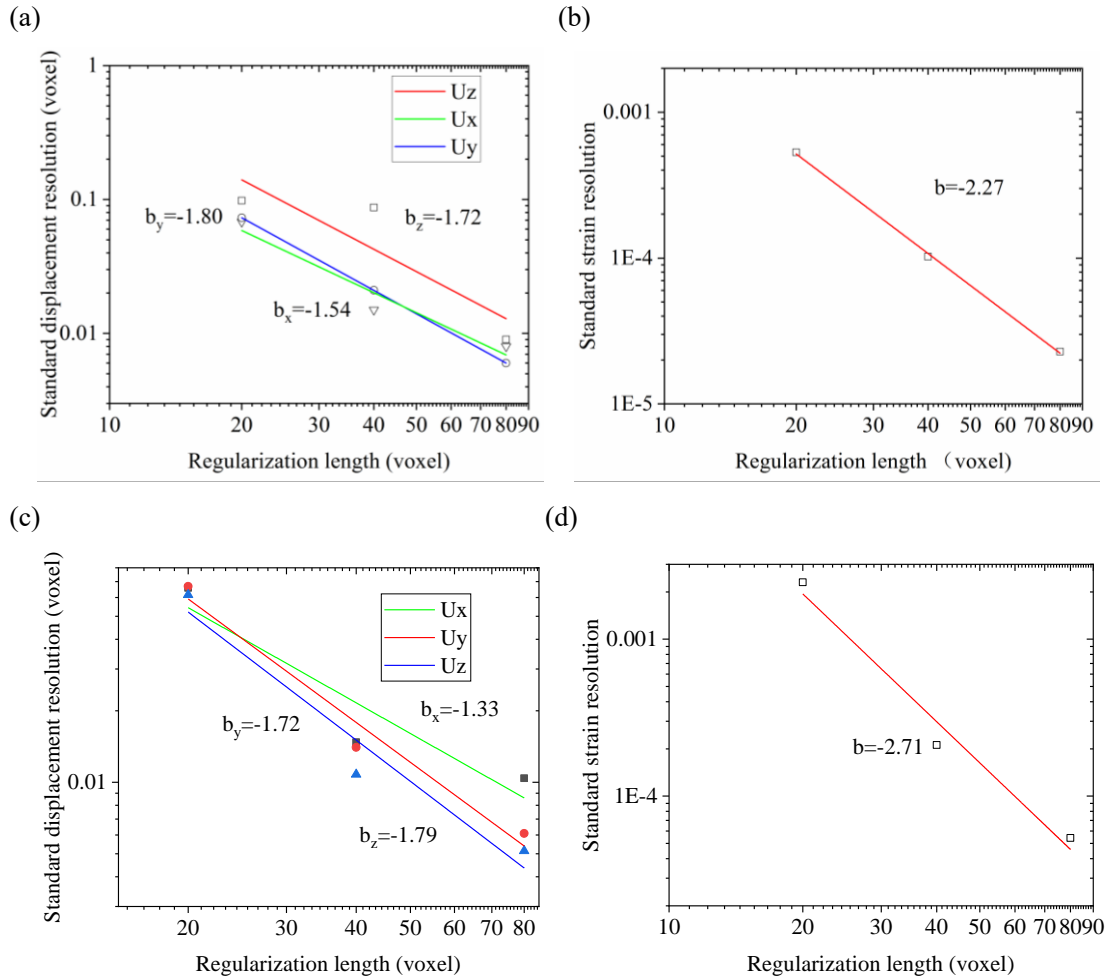
286

3.2 Uncertainty Analysis

Considering the effect of noise during the scanning process and reconstruction artifacts, the first scan (with a pulling force of 0 N) and the second scan (with a pulling force of 126 N) of the matrix area, as shown in Fig. 5(a), were used as the reference and deformed images, respectively, to evaluate the measurement uncertainty of the cementitious matrix. For the fiber, because two images of the fiber in the unloaded state were not acquired, the gray level residual between the two scans of the matrix in the unloaded state was regarded as noise. This noise was added to the reference image to generate a ‘deformed image,’ and the measurement uncertainty was assessed for these two volumes.

Using Reg-G-DVC, the element size was set to 5 voxels, and regularization lengths of 80, 40, and 20 voxels were selected. Fig. 6(a) and (b) show the variations in standard displacement uncertainties for the matrix along the x -, y -, and z -directions, and maximum principal strain uncertainties in a double-logarithmic plot when increasing the regularization length. The scattered points represent the measured values, and the dashed lines depict the fitted curve (with a power law). According to theoretical analyses [47], the value of the exponent b corresponding to displacement uncertainties is -1.5 , and that corresponding to maximum the standard principal strain uncertainty is -2.5 . It is found from Fig. 6(a) and (b) that the exponents approach the predicted values. As the regularization length was increased, both standard uncertainties decreased (faster for the strains wrt. the displacements). The uncertainty levels in the three directions were generally similar.

Fig. 6(c) and (d) show the variations in standard displacement and maximum principal strain uncertainties of the fiber in a double-logarithmic coordinate system when increasing the regularization length. The general trends are similar to those in the matrix.



316 Fig. 6 Uncertainties vs. regularization length. The colored lines depict power law interpolations.

317 (a) Standard displacement uncertainties in the matrix, (b) Corresponding maximum principal
 318 strain uncertainty. (c) Standard displacement uncertainties in the fiber, (d) Corresponding
 319 maximum principal strain uncertainty.

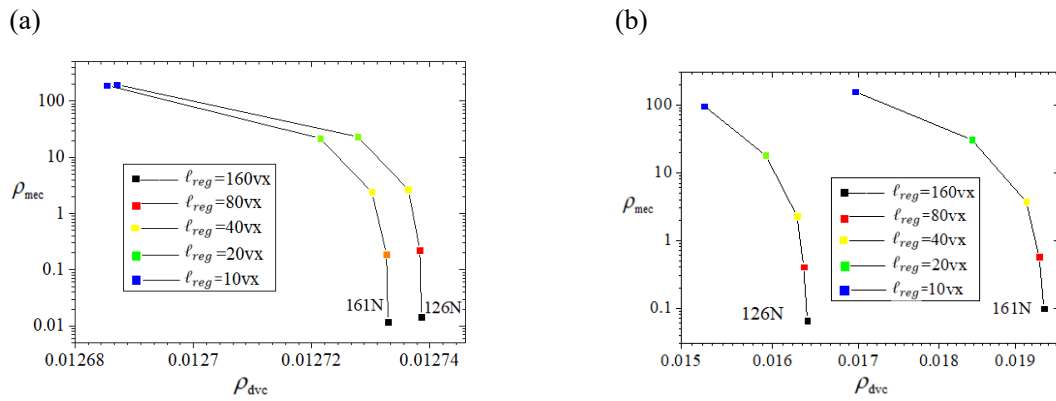
320

321 The numerical values of the standard displacement uncertainties σ of fiber and matrix
 322 obtained using Reg-G-DVC were equal to 0.01 voxels and 0.05 voxels, respectively, when the
 323 regularization length was set to 40 voxels.

324 3.3 DVC Parameters

325 The VOI is shown in Fig. 4(a). To obtain high-spatial-resolution deformation fields for
 326 analyzing the kinematics at the interface between the fiber and the cementitious matrix, a small
 327 element size was selected. Reducing the element size may increase the measurement uncertainty,
 328 even result in divergence in DVC calculations. In the present case, when the mesh size was set to

329 $5 \times 5 \times 5$ voxels, the calculations did not converge with classical (i.e., unregularized) DVC.
330 However, “regularization relaxation” steps were employed in the Reg-G-DVC calculations to ensure
331 that the initial displacements at each iteration were within reasonable ranges. It consisted in first
332 enforcing the largest regularization length. Once DVC had converged, the next DVC step was run
333 with a lower regularization as well as initialized with the previous solution, and so on. Reg-G-DVC
334 calculations were performed separately for the selected cementitious matrix and fiber regions of
335 interest determined during the uncertainty analysis to select an appropriate regularization length.
336 The microtomography images obtained at a load of 0 N were used as the reference volume, whereas
337 those acquired at force levels of 126 and 161 N were used as deformed volumes. The mechanical
338 residual $\rho_{mec} = \sqrt{\Phi_m^2}$ and the correlation residual ρ_{dvc} in the matrix and the fiber under different
339 loads and regularization lengths were computed (Fig. 7).



340 Fig. 7 Mechanical residual ρ_{mec} and correlation residual ρ_{dvc} under different loads and
341 regularization lengths. (a) Matrix. (b) Fiber.

342
343 As shown in Fig. 7(a) and (b), the mechanical residual decreased significantly as the
344 regularization length ℓ_{reg} increased, whereas the gray level residual changed less, which means
345 that the hypothesis of elasticity was satisfied in both constituents. For the matrix and fiber, when
346 ℓ_{reg} decreased from 160 to 10 voxels, the increment of the gray level residual was only 10^{-5} and
347 10^{-3} . Therefore, a large regularization length ℓ_{reg} can be selected for the DVC calculations.
348 However, the fiber cross-sectional thickness was only 0.66mm (approximately 35 voxels), and
349 extremely high values may cause the fiber deformation to be overly smooth. In the following,
350 $\ell_{reg} = 40$ voxels was chosen.

351 **4 DVC Results and Debonding Analysis**

352 Reg-G-DVC was utilized to measure the internal displacement and strain fields of the tested
353 specimen during various stages of fiber pullout. The kinematic fields are first discussed and
354 followed by a quantitative analysis of debonding. The calculation region is shown in Fig. 5(a).

355 **4.1 Deformation Field Analysis**

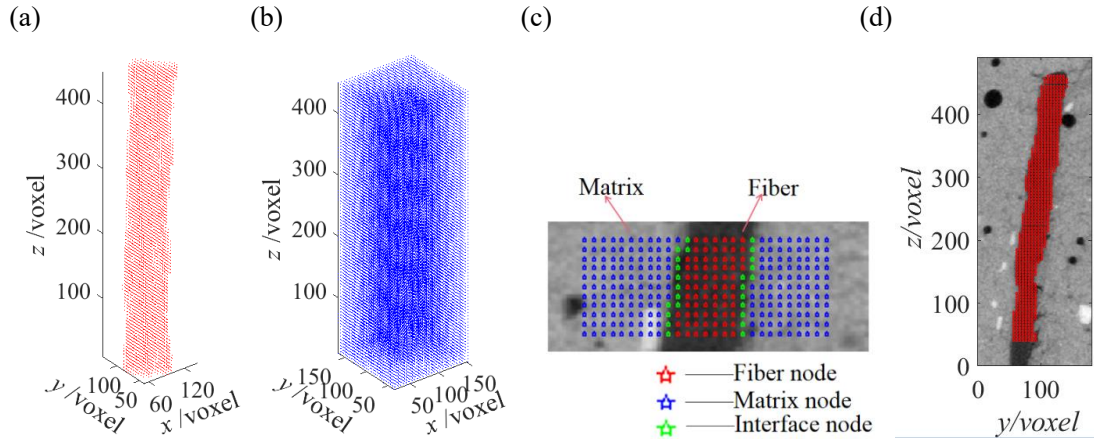
356 To analyze debonding at the fiber–matrix interface during the pullout process, a separate
357 calculation strategy was adopted in which DVC analyses were performed independently for the fiber
358 and the matrix. The microtomography images obtained at a loading of 0 N were used as the reference
359 volume, whereas those acquired at loading levels of 126 and 161 N were used as the deformed
360 volumes. The specific steps were as follows:

361 (1) *Image Segmentation*. The reference microtomography image corresponding to the
362 reference volume was segmented into fiber and matrix regions using Fiji software [51]. The image
363 contrast was enhanced using image enhancement tools, an appropriate threshold was selected for
364 binarization, and morphological post-processing was applied to the segmented image. A series of
365 erosions followed by dilations was used as opening operations to smoothen the fiber boundary
366 voxels. After segmentation, the gray levels of the fiber region were set to 255, and the matrix region
367 was set to 0. The binarized image served as template for the subsequent region-based DVC
368 calculation.

369 (2) *Regional DVC Calculations*. The regions containing both the fiber and matrix were
370 discretized into elements with a size of $5 \times 5 \times 5$ voxels. The regularization lengths were set to 80
371 and 40 voxels, respectively. The templates obtained from image segmentation of Step (1) were used
372 to determine the corresponding elements and nodes for the fiber/matrix regions. The fiber and matrix
373 comprised 4,123 and 52,661 elements, respectively. Separate DVC calculations were conducted for
374 these two regions.

375 (3) *Debonding Analysis*. Based on the results obtained from the region-based DVC calculations
376 of Step (2), the displacement jumps at the fiber–matrix interface (split) nodes i.e., their relative
377 displacements, were determined. This analysis allowed the debonding process at the interface to be
378 quantified.

379 Schematic diagrams of the fiber and matrix elements are shown in Fig. 8(a) and (b),
 380 respectively. The split nodes at the fiber–matrix interface are displayed in Fig. 8(c), where the blue
 381 and red markers represent nodes in the matrix and fiber region, respectively, whereas the green
 382 markers depict the split nodes at the interface. Interfacial debonding is examined by analyzing the
 383 relative motions of the split nodes.



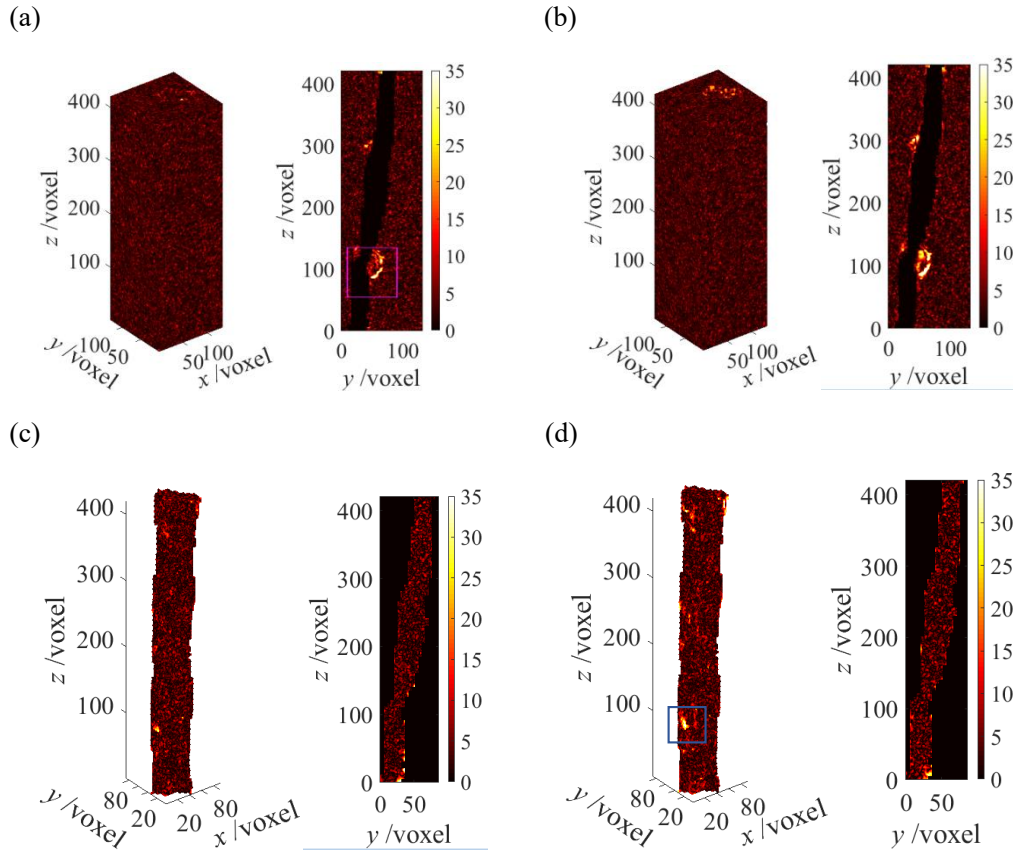
384 Fig. 8 Definition of the various nodes. (a) Fiber, (b) Matrix, (c) Interface. (d) Fiber node locations
 385

386 Fig. 8(d) shows the nodes within the fiber region for a yOz section corresponding to
 387 $x = 90$ voxels in the reference configuration. The segmented region was deemed accurate, and the
 388 nodes at the fiber–matrix interface coincided with the actual interface.

389 The gray-level residual fields of the matrix and fiber obtained using Reg-G-DVC for pulling
 390 forces of 126 and 161 N are shown in Fig. 9(a) and (d). For both scans, their value is of the order of
 391 3 gray levels in the matrix, whereas they reached ca. 4 gray levels within the fiber. The fact that the
 392 gray-level residuals remained very small allowed us to deem the DVC registrations successful. In
 393 addition, as shown in Fig. 9(a) and (b), the residuals in some areas of the matrix near the interface
 394 were greater than those in other areas, such as the magenta box area. When $F = 126$ N, the order of
 395 magnitude of the residuals was 10 voxels, and when $F = 161$ N, the residuals reached 20 voxels.
 396 This observation indicates that damage may have occurred in that area of the matrix, and damage
 397 grew with the increase in pulling force. The elements in that region did not satisfy the assumption
 398 of elasticity in the mechanical regularization term. This issue can be addressed by introducing a
 399 damage variable to reduce the weight of the penalization, thereby enhancing the accuracy of the
 400 DVC results [52]. From Fig. 9(c) and (d), it is observed that some areas in the fiber near the interface
 401 had large residuals, such as the blue box area, which may be due to the fact that the segmented fiber

402 contained a small amount of matrix.

403



404 Fig. 9 Gray-level residual fields. In the matrix when $F = 126$ N (a) and $F = 161$ N (b);

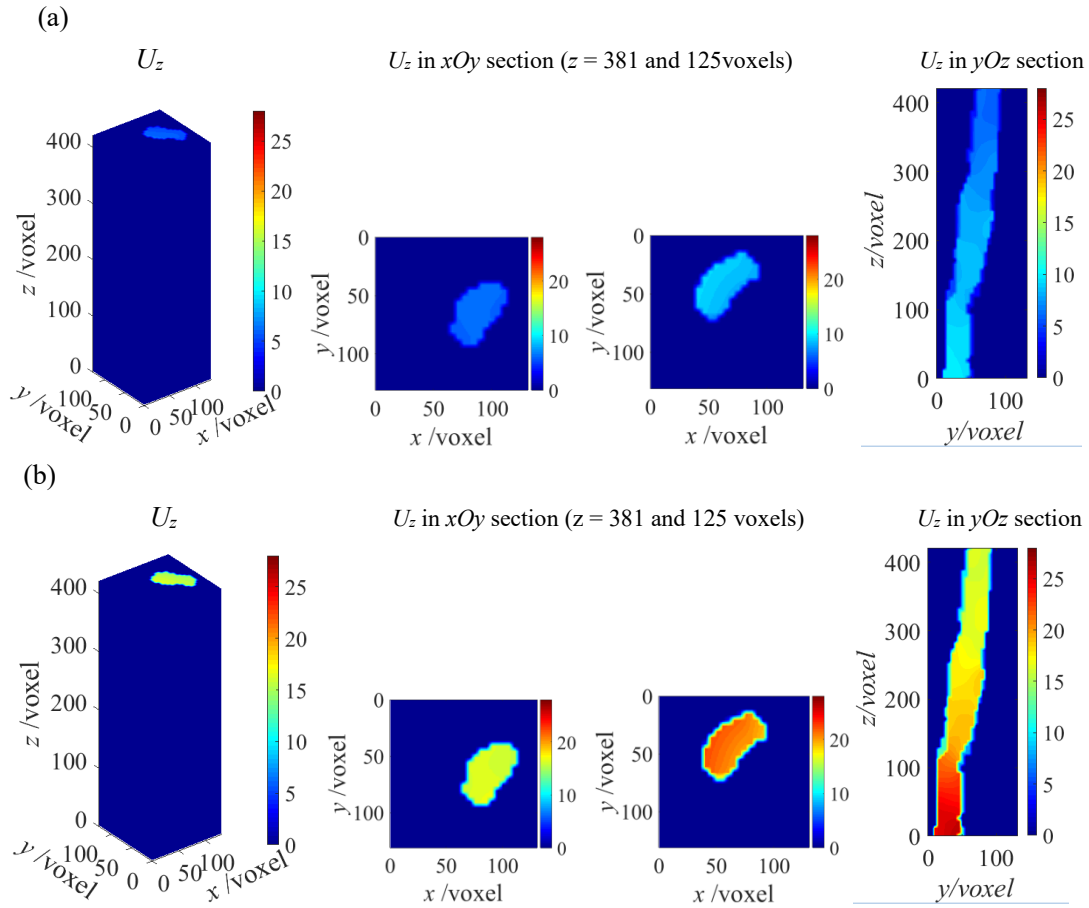
405 in the fiber when $F = 126$ N (c) and $F = 161$ N (d).

406

407 The combined displacement fields of both regions (including the split nodes) after rigid body
408 rotation and translation corrections are shown in Fig. 10. From Fig. 10(a), it is observed that when
409 the pulling force was equal to 126 N, the fiber experienced approximately 6 voxels (0.11 mm) of
410 displacement at the embedded end, and about 12 voxels (0.23 mm) at the initiation region. As shown
411 in Fig. 10(b), when the pulling force was equal to 161 N, the fiber underwent about 16 voxels
412 (0.30 mm) of motion at the embedded end, and approximately 28 voxels (0.53mm) at the initiation
413 region. It was expected that the displacements at the initiation region were greater than at the
414 embedded end. Furthermore, when the fiber was subjected to a downward pulling force, there was
415 an overall downward displacement, and this displacement increased with higher pulling force.

416

417



418 Fig. 10 Displacement fields in the z -direction expressed in voxels when the pulling force is equal
 419 to (a) 126 N and (b) 161 N.

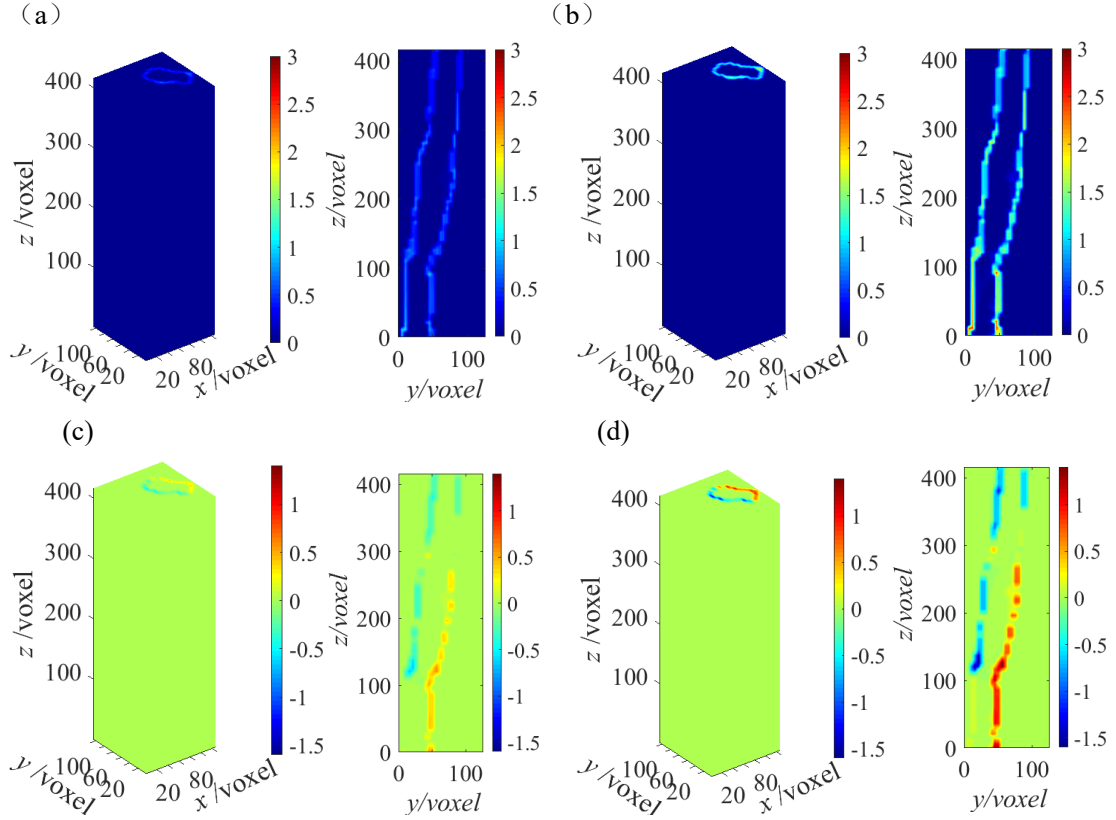
420

421 Based on the displacement fields obtained from separate calculations, the strain fields were
 422 computed by differentiating the finite-element shape-functions. Fig. 11 shows three-dimensional
 423 and sectional views of the maximum principal strain and shear strain fields. From Fig. 11(a) and (b),
 424 it is observed that significant strains occurred at the interface during fiber pullout. Under a pulling
 425 force of 126N, the strain distribution was relatively uniform. When the pulling force increased to
 426 161N, the strain levels increased, and it is observed that the strains were higher at some positions,
 427 which was due to the presence of indentations on the fiber surface. From Figs. 11(c) and (d), it is
 428 seen that the shear strain ϵ_{xz} distribution at the interface was uneven. This observation may
 429 indicate an uneven distribution of interfacial bonding strength along the pull-out direction.

430

431

432



433 Fig. 11. Strain fields. Maximum principal strain when $F = 126$ N (a) and $F = 161$ N. Shear strain
 434 ϵ_{xz} when $F = 126$ N (c) and $F = 161$ N (d).

435 4.2 Debonding Analysis

436 To analyze the debonding process during fiber pullout from the matrix, the displacement jump
 437 of the split nodes is defined as

$$438 \quad d\mathbf{U} = \mathbf{U}_{\text{fiber}} - \mathbf{U}_{\text{matrix}} \quad (15)$$

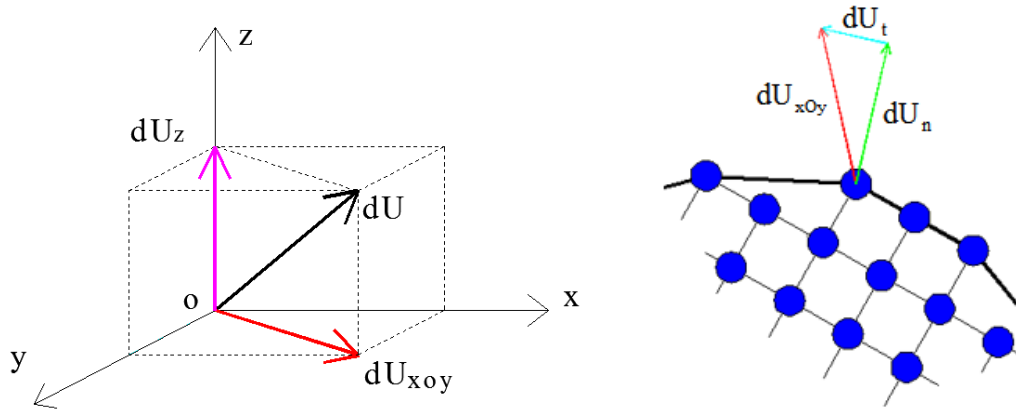
439 To assess the debonding conditions, the displacement jump vector $d\mathbf{U}$ is decomposed into vertical
 440 (z -axis) dU_z and horizontal (within the xOy plane) $d\mathbf{U}_{xoy}$ components; $d\mathbf{U}_{xoy}$ is decomposed

441 into dU_t and dU_n (Fig. 12), where dU_n and dU_t are the displacement jumps along the
 442 normal and tangential directions of the fiber surface in the xOy plane (slice plane), respectively.

443 When analyzing debonding, the measurement uncertainty was considered to avoid false alarms (i.e.,
 444 detecting debonded nodes in the repeat scans). The same volumes as in Section 3.2 were used to
 445 evaluate the standard uncertainty of the displacement jump components. The results are as follows:

446 $\sigma_{dU_n} = 0.06$, $\sigma_{dU_t} = 0.09$ and $\sigma_{dU_z} = 0.04$ voxel. The debonding threshold was selected as five times

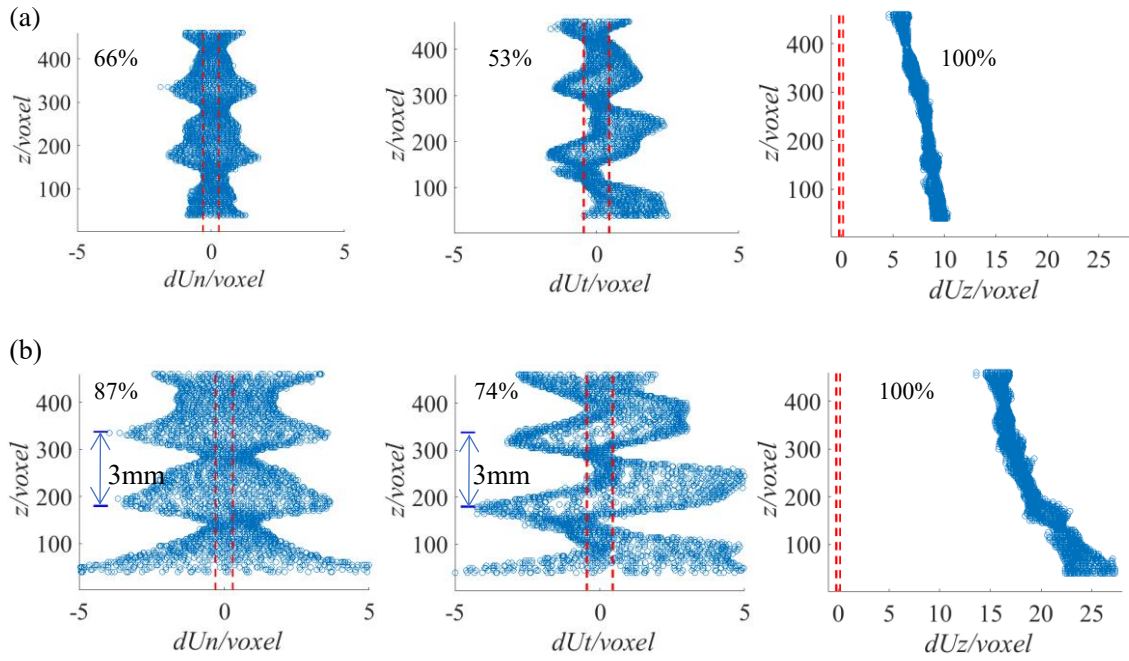
447 the uncertainty of the displacement jump component [50]. Thus, the detection thresholds for dU_n ,
 448 dU_t , and dU_z are equal to 0.3, 0.45 and 0.2 voxel, respectively. The nodes with the displacement
 449 jump exceeding the detection threshold are assumed to be debonded.
 450



451 Fig. 12. Decomposition dU into z -direction and normal and tangential displacement jumps in the
 452 xOy plane.
 453

454 In Fig. 13, the distribution of normal, tangential and longitudinal displacement jumps are
 455 presented for pullout forces equal to 126 and 161 N. The horizontal axis represents the displacement
 456 jump of nodes, while the vertical axis represents the position of the node in the longitudinal
 457 (z -)direction. The displacement jumps of the nodes outside the two dashed red lines were greater
 458 than the detection threshold, and they were labeled as debonded. The percentage in the figures
 459 reports that of debonded nodes relative to the total number of split nodes. It is observed that the
 460 normal and tangential displacement jumps within were unevenly distributed and related to the
 461 geometric shape of the fiber. The indentation spacing was 158 voxels, which corresponded to 3 mm,
 462 and the interval between significant changes in displacement jump was approximately 3 mm as well.
 463 This feature was more pronounced when the pulling force reached 161 N. When the pulling force
 464 was equal to 126 N, the longitudinal displacement jump varied between 4.6 and 10.3 voxels, which
 465 was at least one order of magnitude higher than the detection threshold, thereby indicating that the
 466 fiber was completely debonded. When the pulling force reached 161N, the longitudinal
 467 displacement jump continued to increase, now ranging from 13.6 to 27.3 voxels.

468
 469



470 Fig. 13 Normal, tangential and longitudinal displacement jumps when the pullout force as equal to
 471 126 N (a) and 161 N (b).

472

473 Fig. 14 shows 3D renderings of displacement jumps along the normal, tangential and
 474 longitudinal directions. Fig.14(a) and (b) show that the normal and tangent displacement jumps are
 475 unevenly distributed, exhibiting positive values on one side of the fiber and negative values on the
 476 other side, with a central region of approximately 0 level. Fig.14(c) indicates that when the pullout
 477 force reached 126 N, 6 to 12 voxels displacement jumps were detected between the fiber and the
 478 matrix. When the pullout force reached 161 N, 16 to 28 voxels displacement jumps were detected,
 479 and the displacement jump from the embedded end to the embedded initiation region of the fiber
 480 gradually increased.

481

482

483

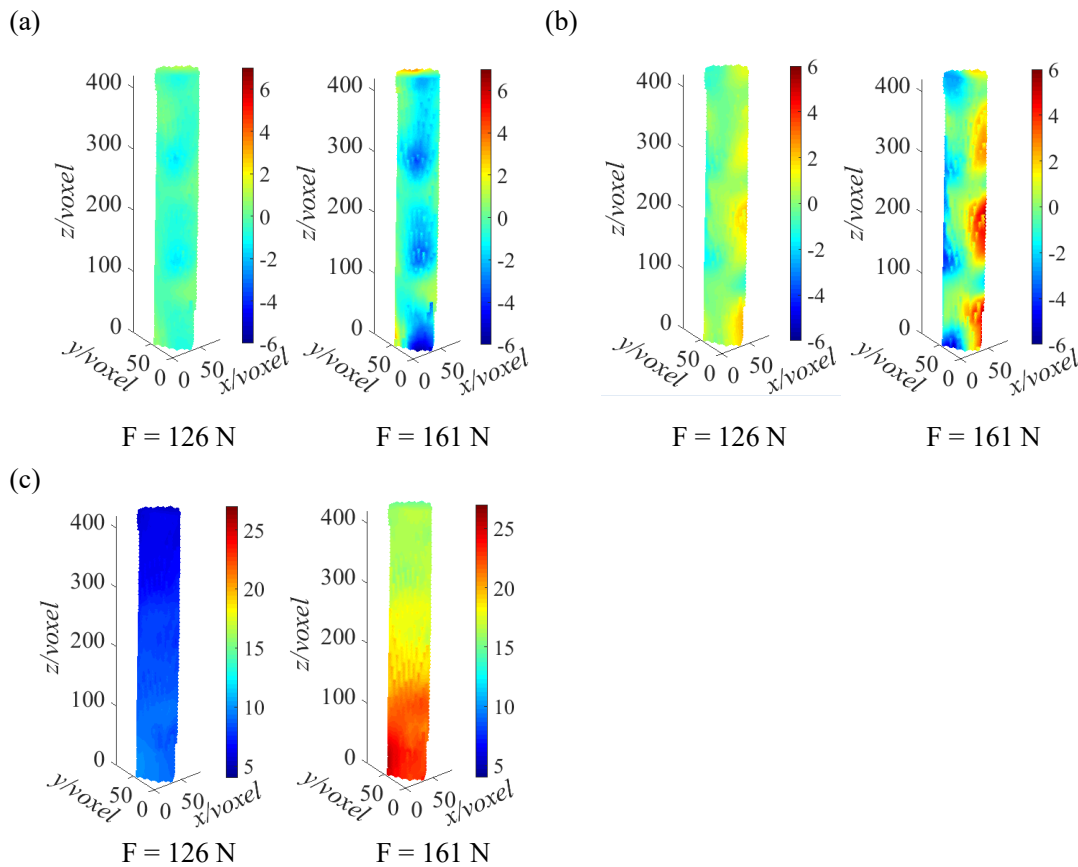
484

485

486

487

488

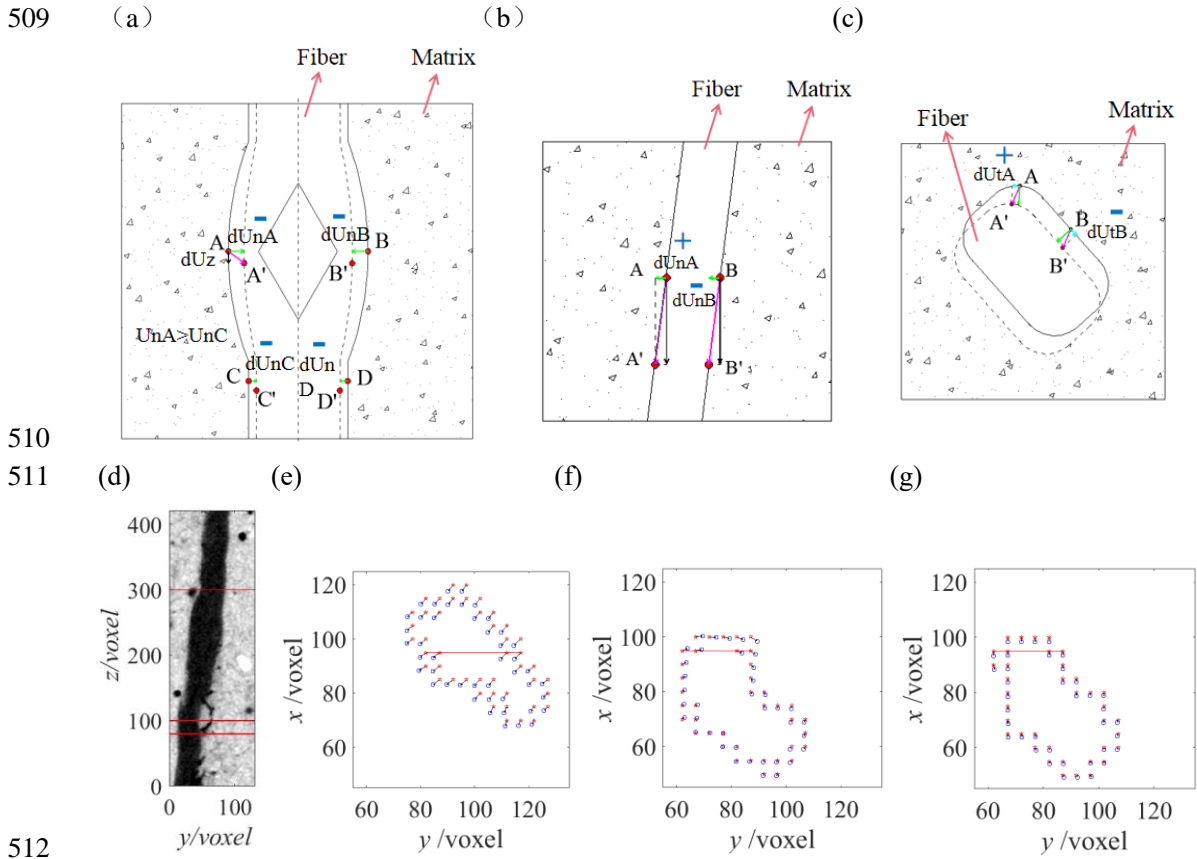


490 Fig. 14 3D renderings of displacement jump fields for the normal (a), tangential (b) and
 491 longitudinal (c) components.

492 Based on the definition of the positive and negative directions of the normal displacement
 493 jumps of the fiber shown in Fig. 12, combined with Fig. 14, it is inferred that the relative motion of
 494 different nodes during fiber pullout was complex. Fig. 15 was drawn for a specific analysis of
 495 Fig. 14(a) and (b). Fig.15(a) and (c) represent schematic diagrams of the fiber pull-out scenario.
 496 Fig. 15(a) shows that if the fiber is vertically embedded and contracts radially during pullout, then
 497 the normal displacement jumps of all nodes within the xOy plane should be negative and the
 498 magnitude is related to the indentation location. Positions with significant indentation (e.g., points
 499 A and B) experienced higher negative normal displacement jumps within the xOy plane, whereas
 500 other positions (e.g., points C and D) underwent lower levels. Owing to the inclined placement of
 501 the fiber, it moved in the direction indicated by the green arrow in Fig. 15(b) during pullout within
 502 the xOy plane, causing the normal displacement jumps within the xOy plane to be positive on one
 503 side (point A) and negative on the other side (point B).

504 The impact of inclined fiber embedding on the tangential displacement jumps in the xOy plane

505 is shown in Fig. 15(c). Under pulling forces $F = 0$ and 161 N, the positions of the fiber in the xOy
 506 section are depicted by the solid and dashed lines, respectively. It is seen that point A on the fiber
 507 will move to point A', and point B will move to point B'. Therefore, the tangential displacement
 508 jumps at points A and B are positive and negative, respectively.



513 Fig. 15 Analysis diagram of normal and tangential displacement jumps in the xOy plane.
 514 (a) Vertical pull-out. (b) Normal relative position and (c) tangential relative position before and
 515 after oblique pull-out. (d) Grayscale image of yOz section. Displacement jumps in xOy sections
 516 when (e) $z = 300$ voxels, (f) $z = 100$ voxels and (g) $z = 80$ voxels.

517
 518 Based on the displacement jumps, typical sections were selected to analyze the reasons for the
 519 uneven distribution of displacement jumps in xOy sections. Fig. 15(d) shows a grayscale image of
 520 the yOz cross-section. The displacement jumps in xOy sections corresponding to three different
 521 heights ($z=300, 100, 80$ voxels) are shown in Fig. 15(e) and (g). The red pentagrams in Fig. 15(e)
 522 and (g) indicate the node positions at a pull-out force $F = 0$ N, while the blue circles indicate the
 523 new positions when $F = 161$ N. In Fig. 15(e), all four nodes on the red line move in the negative y -
 524 direction due to the inclination of the fiber toward the negative y -axis. In Fig. 15(f), all four nodes

525 on the red line move along the positive y -direction due to the inclination of the fiber toward the
526 positive y -axis. In Fig. 15(g), the four nodes on the red line experienced minimal motion in the y -
527 direction, indicating that there was no inclination of the fiber at that location.

528 **5 Conclusion**

529 In this study, the interface between polypropylene fibers (typically used as synthetic
530 reinforcement) and concrete was investigated. Mechanically regularized DVC was employed to
531 perform three-dimensional quantifications of the development of interface debonding during an in-
532 situ pullout test. The main conclusions were as follows:

533 (1) Reg-G-DVC incorporates mechanical regularization, thereby enhancing the spatial
534 resolution of displacement measurements. When the element size was reduced to as low as 5 voxels,
535 and the regularization length was set to 40 voxels, the maximum standard displacement uncertainties
536 for the mortar matrix and the fiber were equal to 0.09 and 0.11 voxels, respectively. The deformation
537 fields of the mortar matrix and fibers during the pre-peak pullout process were captured. Pronounced
538 strain concentrations were observed at the interface, revealing the deformation characteristics of the
539 interface.

540 (2) Debonding of the interface could be effectively analyzed by using the normal and tangential
541 displacement jumps and the relative displacement along the fiber direction at the split nodes between
542 the fiber and the matrix. The distribution of normal and tangential displacement jumps exhibited
543 periodic fluctuations corresponding to the fiber geometry. The maximum displacement jump along
544 the fiber occurred at the embedded initiation, and it decreased along the fiber toward the embedded
545 end. As the pull-out force increased, the debonding zone extended from the embedded initiation to
546 the embedded end of the fiber.

547 (3) The indentations on the fiber surface caused the fiber size to change periodically along the
548 length, which significantly affected both macroscopic and microscopic characteristics obtained from
549 the analysis of an in-situ fiber pullout test. The force–displacement curve showed multippeak features
550 beyond the ultimate force, and the displacement jumps along the fiber surface in the normal and
551 tangential directions had periodic fluctuations corresponding to the indentation spacing. This
552 observation indicates that the periodic indentation on the fiber enhanced the friction and cohesive
553 forces between the fiber and the matrix during the pull-out process. In addition, the influence of

554 fiber geometry on pull-out was also observed through the strain distribution at the interface, where
555 significant strain concentrations existed at locations with smaller fiber cross-sectional widths.

556 This study demonstrated the feasibility and advantages of using Reg-G-DVC to measure and
557 analyze displacement fields during interface debonding. Additionally, it provided quantitative
558 support for validating interface models and identifying full-field deformation parameters by
559 utilizing this research framework to obtain deformation data.

560

561 **Funding:** This work was financially supported by Science Fund for Creative Research Groups of
562 the National Natural Science Foundation of China (52121003), and the National Key Research and
563 Development Program of China (2022YFC2904102).

564 **Conflicts of interest:** The authors declare no conflict of interest.

565 **CRedit author statement:** **Yujie Bi:** Conceptualization, Methodology, Investigation, and Writing-
566 Original Draft. **Haizhou Liu:** Methodology, Software and Investigation; **Lingtao Mao:** Resources,
567 Conceptualization, Validation, Supervision and Writing-Review & Editing; **JiaoJiao Liu:** Formal
568 analysis and Investigation; **Yifan Liu:** Formal analysis and Resources; **Jianmin Zuo:** Resources; **Yang**
569 **Ju:** Funding acquisition and Supervision; **François Hild:** Conceptualization, Methodology, Validation,
570 and Writing-Review.

571

572 **References**

- 573 1. Marcinkiewicz K, Wells M (2014) Staircase showcase for ultra-high-strength fibre-reinforced
574 concrete. *Proceedings of the Institution of Civil Engineers-Civil Engineering*, 167(3): 131-137.
575 <https://doi.org/10.1680/cien.14.00003>
- 576 2. Kadhim A M H, Numan H A, Ozakca M (2019) Flexural strengthening and rehabilitation of
577 reinforced concrete beam using BFRP composites: finite element approach. *Advances in Civil*
578 *Engineering*, 2019. <https://doi.org/10.1155/2019/4981750>
- 579 3. Benzecry V, Rossini M, Morales C et al (2021) Design of marine dock using concrete mixed with
580 seawater and FRP bars. *Journal of Composites for Construction*, 25(1).
581 [https://doi.org/10.1061/\(asce\)cc.1943-5614.0001100](https://doi.org/10.1061/(asce)cc.1943-5614.0001100)
- 582 4. Domingo M, Ramos G, Aparicio A C (2023) Use of fiber reinforced concrete in bridges-Metrorrey
583 Line 2 case study. *Engineering Structures*, 276. <https://doi.org/10.1016/j.engstruct.2022.115373>
- 584 5. Mulheron M, Kevren J T, Rupnow T D (2015) Laboratory fatigue and toughness evaluation of
585 fiber-reinforced concrete. *Transportation Research Record*, (2508): 39-47.
586 <https://doi.org/10.3141/2508-05>
- 587 6. Ge Z S, Wang H, Zhang Q S et al (2015) Glass fiber reinforced asphalt membrane for interlayer

588 bonding between asphalt overlay and concrete pavement. *Construction and Building Materials*,
589 101: 918-925. <https://doi.org/10.1016/j.conbuildmat.2015.10.145>

590 7. Carmona S, Molins C, Aguado A et al (2016) Distribution of fibers in SFRC segments for tunnel
591 linings. *Tunnelling and Underground Space Technology*, 51: 238-249.
592 <https://doi.org/10.1016/j.tust.2015.10.040>

593 8. Cui G Y, Wang X L, Wang D Y (2020) Study on the model test of the antibreaking effect of fiber
594 reinforced concrete lining in tunnel. *Shock and Vibration*, 2020.
595 <https://doi.org/10.1155/2020/5419650>

596 9. Zhang H, Cao S, Yilmaz E (2022) Influence of 3D-printed polymer structures on dynamic splitting
597 and crack propagation behavior of cementitious tailings backfill. *Construction and Building*
598 *Materials*, 343. <https://doi.org/10.1016/j.conbuildmat.2022.128137>

599 10. Li J J, Cao S, Yilmaz E (2024) Reinforcing effects of polypropylene on energy absorption and
600 fracturing of cement-based tailings backfill under impact loading. *International Journal of Minerals*
601 *Metallurgy and Materials*, 31(4): 650-664. <https://doi.org/10.1007/s12613-023-2806-3>

602 11. Li Q, Dong Z (2001) Some developments on meso-mechanics of fiber-reinforced quasi-brittle
603 composites. *Advances in Mechanics*, 31: 555-582. <https://doi.org/10.6052/1000-0992-2001-4->
604 [J2001-010](https://doi.org/10.6052/1000-0992-2001-4-J2001-010)

605 12. Abu-Lebdeh T, Hamoush S, Heard W et al (2011) Effect of matrix strength on pullout behavior
606 of steel fiber reinforced very-high strength concrete composites. *Construction and Building*
607 *Materials*, 25(1): 39-46. <https://doi.org/10.1016/j.conbuildmat.2010.06.059>

608 13. Hong L, Li T D, Chen Y D et al (2020) Characteristics of Interfacial Shear Bonding Between
609 Basalt Fiber and Mortar Matrix. *Materials*, 13(21). <https://doi.org/10.3390/ma13215037>

610 14. She P, Wang J, Pang Z et al (2022) A Unified Model for Fibers With Divergent Pullout Behaviors
611 in Strain Hardening Cementitious Composites (SHCC). *Frontiers in Materials*, 9.
612 <https://doi.org/10.3389/fmats.2022.860113>

613 15. Liu X, Sun Q H, Yuan Y et al (2020) Comparison of the structural behavior of reinforced concrete
614 tunnel segments with steel fiber and synthetic fiber addition. *Tunnelling and Underground Space*
615 *Technology*, 103. <https://doi.org/10.1016/j.tust.2020.103506>

616 16. Huang L, Yuan M, Wei B D et al (2022) Experimental investigation on sing fiber pullout
617 behaviour on steel fiber-matrix of reactive powder concrete (RPC). *Construction and Building*
618 *Materials*, 318. <https://doi.org/10.1016/j.conbuildmat.2021.125899>

619 17. Wu Z M, Shi C J, He W et al (2016) Effects of steel fiber content and shape on mechanical
620 properties of ultra high performance concrete. *Construction and Building Materials*, 103: 8-14.
621 <https://doi.org/10.1016/j.conbuildmat.2015.11.028>

622 18. Breitenbuecher R, Meschke G, Song F et al (2014) Experimental, analytical and numerical
623 analysis of the pullout behaviour of steel fibres considering different fibre types, inclinations and
624 concrete strengths. *Structural Concrete*, 15(2): 126-135. <https://doi.org/10.1002/suco.201300058>

625 19. Isla F, Arganaraz P, Luccioni B (2022) Numerical modelling of steel fibers pull-out from
626 cementitious matrixes. *Construction and Building Materials*, 332.
627 <https://doi.org/10.1016/j.conbuildmat.2022.127373>

628 20. Jamshaid H, Mishra R K, Raza A et al (2022) Natural cellulosic fiber reinforced concrete:
629 influence of fiber type and loading percentage on mechanical and water absorption performance.
630 *Materials*, 15(3). <https://doi.org/10.3390/ma15030874>

631 21. Hussain I, Ali B, Akhtar T et al (2020) Comparison of mechanical properties of concrete and

632 design thickness of pavement with different types of fiber-reinforcements (steel, glass, and
633 polypropylene). *Case Studies in Construction Materials*, 13: e00429.
634 <https://doi.org/https://doi.org/10.1016/j.cscm.2020.e00429>

635 22. Kos Z, Kroviakov S, Kryzhanovskiy V et al (2022) Strength, Frost Resistance, and Resistance to
636 Acid Attacks on Fiber-Reinforced Concrete for Industrial Floors and Road Pavements with Steel
637 and Polypropylene Fibers. *Materials*, 15(23). <https://doi.org/10.3390/ma15238339>

638 23. Li C, Chen X, Zhang X et al (2023) Interface mechanical bonding properties between coarse
639 synthetic polypropylene fiber and cement mortar. *Acta Materiae Compositae Sinica*, 40(4): 2427.
640 <https://doi.org/10.13801/j.cnki.fhclxb.20220624.001>

641 24. Shan J H, Zhou M, Li B X et al, Application of polypropylene fiber concrete in bridge deck
642 pavement, in: N.Q. Feng, G.F. Peng (Eds.), *Environmental Ecology and Technology of Concrete2006*,
643 pp. 418-423. <https://doi.org/10.4028/www.scientific.net/KEM.302-303.418>

644 25. Behfarnia K, Behravan A (2014) Application of high performance polypropylene fibers in
645 concrete lining of water tunnels. *Materials & Design*, 55: 274-279.
646 <https://doi.org/10.1016/j.matdes.2013.09.075>

647 26. Cao S, Xue G L, Yilmaz E et al (2021) Utilizing concrete pillars as an environmental mining
648 practice in underground mines. *Journal of Cleaner Production*, 278.
649 <https://doi.org/10.1016/j.jclepro.2020.123433>

650 27. Sato M, Imai E, Koyanagi J et al (2017) Evaluation of the interfacial strength of carbon -fiber-
651 reinforced temperature-resistant polymer composites by the micro-droplet test. *Advanced*
652 *Composite Materials*, 26(5): 465-476. <https://doi.org/10.1080/09243046.2017.1284638>

653 28. Garnevicus M, Plioplys L, Ng P L et al (2020) Investigation and Improvement of Bond
654 Performance of Synthetic Macro-Fibres in Concrete. *Materials*, 13(24).
655 <https://doi.org/10.3390/ma13245688>

656 29. Wang L H, Li T S, Shu Q H et al (2023) Experimental Study of Fiber Pull-Outs in a Polymer
657 Mortar Matrix. *Materials*, 16(9). <https://doi.org/10.3390/ma16093594>

658 30. Odendaal C M, Babafemi A J, Combrinck R et al (2018) Evaluation of locally available synthetic
659 macro fibres in a single-fibre pullout test in concrete. *Journal of the South African Institution of*
660 *Civil Engineering*, 60(1): 21-30. <https://doi.org/10.17159/2309-8775/2018/v60n1a3>

661 31. Vazquez-Rodriguez J M, Herrera-Franco P J, Gonzalez-Chi P I (2007) Analysis of the interface
662 between a thermoplastic fiber and a thermosetting matrix using photoelasticity. *Composites Part*
663 *a-Applied Science and Manufacturing*, 38(3): 819-827.
664 <https://doi.org/10.1016/j.compositesa.2006.08.003>

665 32. Rjafiallah S, Guessasma S (2011) Three-phase model and digital image correlation to assess
666 the interphase effect on the elasticity of carbohydrate polymer-based composites reinforced with
667 glass-silica beads. *Carbohydrate Polymers*, 83(1): 246-256.
668 <https://doi.org/https://doi.org/10.1016/j.carbpol.2010.07.055>

669 33. Hamrat M, Boulekbache B, Chemrouk M et al (2016) Flexural cracking behavior of normal
670 strength, high strength and high strength fiber concrete beams, using Digital Image Correlation
671 technique. *Construction and Building Materials*, 106: 678-692.
672 <https://doi.org/10.1016/j.conbuildmat.2015.12.166>

673 34. Skarzynski L, Suchorzewski J (2018) Mechanical and fracture properties of concrete reinforced
674 with recycled and industrial steel fibers using Digital Image Correlation technique and X-ray micro
675 computed tomography. *Construction and Building Materials*, 183: 283-299.

676 <https://doi.org/10.1016/j.conbuildmat.2018.06.182>

677 35. Hao W, Tang C, Yuan Y et al (2015) Experimental study on the fiber pull-out of composites
678 using digital gradient sensing technique. *Polymer Testing*, 41: 239-244.
679 <https://doi.org/10.1016/j.polymertesting.2014.12.005>

680 36. Ren W, Yang Z, Sharma R et al (2018) Three-dimensional in situ XCT characterisation and FE
681 modelling of cracking in concrete. *Complexity*. <https://doi.org/10.1155/2018/3856584>

682 37. Bennai F, El Hachem C, Abahri K et al (2018) Microscopic hydric characterization of hemp
683 concrete by X-ray microtomography and digital volume correlation. *Construction and Building*
684 *Materials*, 188: 983-994. <https://doi.org/10.1016/j.conbuildmat.2018.08.198>

685 38. Kim J-S, Chung S-Y, Han T-S et al (2020) Correlation between microstructural characteristics
686 from micro-CT of foamed concrete and mechanical behaviors evaluated by experiments and
687 simulations. *Cement & Concrete Composites*, 112.
688 <https://doi.org/10.1016/j.cemconcomp.2020.103657>

689 39. Bay B K, Smith T S, Fyhrie D P et al (1999) Digital volume correlation: Three-dimensional strain
690 mapping using X-ray tomography. *Exp Mech*, 39(3): 217-226.
691 <https://doi.org/10.1007/BF02323555>

692 40. Mao L T, Zhu Y, Wang Y W et al (2020) An improved digital volumetric speckle photography
693 technique with X-ray microtomography and its applications to investigating strain localization in
694 red sandstone. *Rock Mechanics and Rock Engineering*, 53(3): 1457-1466.
695 <https://doi.org/10.1007/s00603-019-01971-w>

696 41. Yang Z, Ren W, Sharma R et al (2017) In-situ X-ray computed tomography characterisation of
697 3D fracture evolution and image-based numerical homogenisation of concrete. *Cement &*
698 *Concrete Composites*, 75: 74-83. <https://doi.org/10.1016/j.cemconcomp.2016.10.001>

699 42. Mao L, Yuan Z, Yang M et al (2019) 3D strain evolution in concrete using in situ X-ray computed
700 tomography testing and digital volumetric speckle photography. *Measurement*, 133: 456-467.
701 <https://doi.org/10.1016/j.measurement.2018.10.049>

702 43. Chateau C, Nguyen T T, Bornert M et al (2018) DVC-based image subtraction to detect
703 microcracking in lightweight concrete. *Strain*, 54(5). <https://doi.org/10.1111/str.12276>

704 44. Stamati O, Roubin E, Ando E et al (2021) Fracturing process of micro-concrete under uniaxial
705 and triaxial compression: Insights from in-situ X-ray mechanical tests. *Cement and Concrete*
706 *Research*, 149. <https://doi.org/10.1016/j.cemconres.2021.106578>

707 45. Flansbjer M, Portal N W, Hall S et al (2018) Analysis of failure modes in fiber reinforced concrete
708 using X-ray tomography and digital volume correlation. *Proceedings*, 2(8): 401.
709 <https://doi.org/10.3390/ICEM18-05238>

710 46. Hild F, Bouterf A, Roux S (2015) Damage measurements via DIC from physical to mechanical
711 damage. *International Journal of Fracture*, 191(1-2): 77-105. [https://doi.org/10.1007/s10704-015-](https://doi.org/10.1007/s10704-015-0004-7)
712 [0004-7](https://doi.org/10.1007/s10704-015-0004-7)

713 47. Leclerc H, Perie J N, Roux S et al (2011) Voxel-scale digital volume correlation. *Experimental*
714 *Mechanics*, 51(4): 479-490. <https://doi.org/10.1007/s11340-010-9407-6>

715 48. Tsitova A, Bernachy-Barbe F, Bary B et al (2022) Damage Quantification via Digital Volume
716 Correlation with Heterogeneous Mechanical Regularization: Application to an In situ Meso-
717 Flexural Test on Mortar. *Experimental Mechanics*, 62(2): 333-349. [https://doi.org/10.1007/s11340-](https://doi.org/10.1007/s11340-021-00778-7)
718 [021-00778-7](https://doi.org/10.1007/s11340-021-00778-7)

719 49. Riccardi F, Giry C, Gatuingt F (2023) Debonding analysis of fibre reinforced polymer anchors in

720 concrete via In-situ X-ray microtomography tests coupled to volume and digital image correlation.
721 Experimental Mechanics, 63(6): 1067-1083. <https://doi.org/10.1007/s11340-023-00975-6>
722 50. Jänicke G, Vintache A, Smaniotto B et al (2022) Debonding analysis via digital volume
723 correlation during in-situ pull-out tests on fractal fibers. Composites Part C: Open Access, 9:
724 100302. <https://doi.org/https://doi.org/10.1016/j.jcomc.2022.100302>
725 51. Schindelin J, Arganda-Carreras I, Frise E et al (2012) Fiji: an open-source platform for
726 biological-image analysis. Nature Methods, 9(7): 676-682. <https://doi.org/10.1038/nmeth.2019>
727 52. Liu H, Mao L, Ju Y et al (2023) Damage evolution in coal under different loading modes using
728 advanced digital volume correlation based on X-ray computed tomography. Energy, 275.
729 <https://doi.org/10.1016/j.energy.2023.127447>
730